Supporting Information

Complex Formation and Dissociation Dynamics on Amorphous Silica Surfaces

Steven A. Yamada[†], Samantha T. Hung[†], Jae Yoon Shin,[§] and Michael D. Fayer[†]*

[§]Department of Advanced Materials Chemistry
Korea University, Sejong, Korea

[†]Department of Chemistry
Stanford University, Stanford, CA 94305, USA
*Phone: (650) 723-4446; Email: fayer@stanford.edu

SI. Optical Methods

A. FTIR Spectroscopy

Linear IR absorption spectra were measured with a Thermo Scientific Nicolet 6700 Fourier Transform IR (FTIR) spectrometer purged with air scrubbed free of CO_2 and H_2O. The measured spectra of Bz, CCl_4, and 1:5 Bz:CCl_4 were scale subtracted from the spectra of MCM41-OD in the same solvents. A small linear baseline correction was included, yielding the spectra of the surface Si-OD stretch in the three solvents.

B. Laser System and Optical Setup.

The 2D IR pulse-shaping spectrometer has been described in detail previously.[1] Briefly, a Ti:sapphire oscillator seeds a regenerative amplifier that outputs 600 μJ pulses at 1 kHz centered at 800 nm with 100 fs full-width at half maximum (FWHM) duration. The regen output pumps an optical parametric amplifier/difference frequency generation (OPA/DFG) system tuned to generate 180 fs (~90 cm^{-1} FWHM bandwidth) mid-IR pulses centered at 2695 cm^{-1} with an energy of 8 μJ. The 2D IR spectrometer is configured in a pump-probe geometry.[1-3] The mid-IR pulses are split into a strong pump and weaker probe pulse (92:8 intensity ratio) with a ZnSe beam splitter. The pump pulse is sent into a mid-IR frequency-domain pulse-shaper consisting of a germanium acousto-optic modulator (AOM) at the Fourier plane of a 4-*f* pulse-shaping geometry.[1, 3, 4] The number, amplitude, phase, and temporal delay of the pump pulse(s) at the output are precisely controlled by the AOM. The probe pulse is sent through a precision mechanical delay stage that sets the time delay between the pump and probe. The two beams are

focused and spatially overlapped in the sample. In the pump-probe geometry, the pump-probe and vibrational echo signals are emitted collinearly with the probe pulse.[2] After the sample, the probe/signal is sent into a monochromator acting as a spectrograph and detected with a liquid nitrogen cooled 32-element HgCdTe (MCT) IR array detector.

C. Polarization-Selective Pump Probe Experiments

Mid-IR PSPP experiments have been discussed in detail previously.[5] Briefly, the pulse sequence involves an intense pump pulse followed by a weaker probe pulse a time, t, later. The pump is chopped (off) at 500 Hz, or half the laser repetition rate. The probe spectrum, acquired when the pump is off, is subtracted from the pump-probe (PP) signal, which is then normalized to the probe spectrum. The AOM controls the chopping rate and the absolute phase of the pump pulse during the on shots to suppress scattered light.[6, 7] For highly scattering samples, an additional phase-cycling procedure was used as previously detailed.[6] Directly before the sample, the probe and pump pulses are fixed at 0° (parallel to the plane of the optical table) and +45° linear polarizations, respectively. Directly following the sample, a polarizer in a computer controlled rotation mount resolves the signal alternately at +45° or -45°, giving the parallel, $S_{\parallel}(t)$, or perpendicular, $S_{\perp}(t)$, PP signals, respectively. These signals have contributions from the isotropic PP signal decay, $P(t)$, and the second order Legendre polynomial orientational correlation function of the transition dipole moment, $C_2(t)$,[8, 9]

$$S_{\parallel}(t) = P(t)[1 + 0.8C_2(t)], \tag{S1}$$

$$S_{\perp}(t) = P(t)[1 - 0.4C_2(t)]. \tag{S2}$$

The signals are then projected back to 0° linear polarization by a final polarizer before being spectrally dispersed and detected with the spectrograph and HgCdTe (MCT) IR array detector. This last polarizer ensures that the signals experience identical grating efficiencies in the spectrograph.

D. 2D IR Spectroscopy

In the 2D IR experiment, two pump pulses (1 and 2) and one probe pulse (3) interact with the sample, stimulating the emission of the vibrational echo signal.[2, 10, 11] The time between

pulses 1 and 2, between 2 and 3, and following 3 are the first coherence period, $t_1 = \tau$, the population period, $t_2 = T_w$, and the final coherence period, t_3. In the pump-probe geometry, the vibrational echo signal is emitted collinearly with pulse 3, which serves as a local oscillator that self-heterodynes the echo, providing information on its phase.[2, 10] The combined echo/LO signal electric field is sent into the spectrograph, which performs an optical Fourier transform of the signal with respect to t_3, generating the ω_3 (vertical) axis of the 2D spectrum. The ω_1 (horizontal) axis is obtained by scanning the delay τ, which generates a temporal interferogram in τ for each ω_3. The interferograms are numerically Fourier transformed to obtain the ω_1 axis, generating the full 2D spectrum.

A complete 2D spectrum is generated by fixing T_w and scanning τ. After this, T_w is incremented and another 2D spectrum is obtained. When 2D IR is applied to a system undergoing chemical exchange, the vibrational frequency evolution during the T_w period will be dictated by two processes: spectral diffusion and chemical exchange.[12]

Spectral diffusion of the silanol (Si-OD) vibrational probe is caused by the structural evolution of the surrounding solvent and silica framework. The structure is coupled to the vibrational frequency, and its evolution determines the T_w-dependence of the diagonal band shape for oscillators that have not exchanged.[12] At early T_w, very little structural evolution has occurred, resulting in a high degree of correlation between the initial (excited) and final (detected) frequencies, ω_1 and ω_3, respectively. The highly correlated spectrum is elongated along the diagonal line $\omega_3 = \omega_1$. As T_w is increased, the initial and final frequencies become increasingly uncorrelated, and the 2D band shape becomes increasingly round. Spectral diffusion is quantified with the frequency-frequency correlation function (FFCF). Here, the FFCF was modeled with the Kubo model[2, 13]

$$\mathrm{FFCF} = \langle \delta\omega(t)\delta\omega(0)\rangle = \sum_i \Delta_i^2 \exp[-t/\tau_i] \tag{S3}$$

where the frequency fluctuation, $\delta\omega(t) = \omega(t) - \langle\omega\rangle$, is the difference between the instantaneous frequency, $\omega(t)$, and the time-averaged frequency, $\langle\omega\rangle$. The i^{th} component of the FFCF is

specified by a frequency fluctuation amplitude, Δ_i, and time constant, τ_i. When $\Delta_i\tau_i \ll 1$, a component is in the homogeneous limit,[2] and Δ_i and τ_i cannot be independently determined. The homogeneous line shape is a Lorentzian with a FWHM given by $\Gamma^* = 1/\pi T_2^*$, where T_2^* is the pure dephasing time.[2] The observed homogeneous dephasing time, T_2, is influenced by T_2^*, the vibrational lifetime, T_1, and the orientational correlation time, T_{or}, according to $(T_2)^{-1} = (T_2^*)^{-1} + (2T_1)^{-1} + (3T_{or})^{-1}$.[11] Components with $\Delta_i\tau_i \gg 1$ are in the inhomogeneous limit,[2] and the line shape is a Gaussian with standard deviation Δ_i. The convolution of the line shapes associated with each component in Eq. (S3) produces the linear absorption spectrum. The spectral diffusion time scales, τ_i, are determined with the ω_3 center-line slope (CLS) method.[14, 15] However, the Δ_i do not directly correspond to the amplitudes in the CLS. The proper Δ_i, in absolute frequency units (cm^{-1}), are determined by reproducing the linear absorption spectrum and CLS decay through response function calculations of the 1D and 2D line shapes.

The second process influencing the vibrational frequency evolution during the T_w period is chemical exchange. Chemical exchange produces off-diagonal peaks that initially increase in amplitude as T_w is increased. The growth of the off-diagonal peaks directly tracks the formation and dissociation of Si-OD/Bz complexes under thermal equilibrium conditions.[12, 16, 17] Following the theoretical discussion of Kwak et al., we assume that chemical exchange destroys all frequency correlation.[12] Consequently, the off-diagonal peaks, which arise from an odd number of exchanges, and the contribution to the diagonal peaks from exchange, which arise from an even number of exchanges, will exhibit completely uncorrelated 2D band shapes. A completely uncorrelated 2D band will have a CLS of zero,[15] and we have verified that this is the case for the off-diagonal peaks in the experimental 2D IR chemical exchange spectra. Note also that the contribution from even exchanges on the diagonal will cause the diagonal features to be more uncorrelated than if no chemical exchange occurred.[12]

The 2D IR experiments were performed with linearly polarized electric fields. To obtain reliable spectra from the strongly light scattering MCM41-OD silica powder, the signal was acquired in the perpendicular polarization configuration, $\langle XXYY \rangle$, in which the first two pulses were vertically polarized (Y) and third pulse and the detected component of the signal were

horizontally polarized (X). The $\langle XXYY \rangle$ signal acts as a polarization filter, since the scatter from the first two pulses is primarily polarized normal to the detection direction. The signal was also acquired using a 4-shot phase cycling scheme that was designed to remove scatter signals originating from the pump pulses.[3, 6, 7]

SII. Heating Signal Subtraction Methods

A. Polarization Selective Pump-Probe Spectroscopy

The pump-probe signals, $S_{\parallel}(t)$ and $S_{\perp}(t)$, for MCM41-OD in pure CCl_4 and pure Bz exhibited a frequency dependent offset at long time delays (Fig. S1). Consequently, an offset is also evident in the un-processed $P(t)$ curves shown in Fig. S2. This feature was previously observed for the OD stretching mode of HOD in H_2O[18, 19] and for the μ_2-OD stretching mode of the metal-organic framework MIL-53(Al).[20] The offset has been attributed to a temperature increase induced by absorption of the pump pulse, or heating signal. This is an unwanted artifact that, if unremoved, leads to an erroneous anisotropy, $r(t)$.

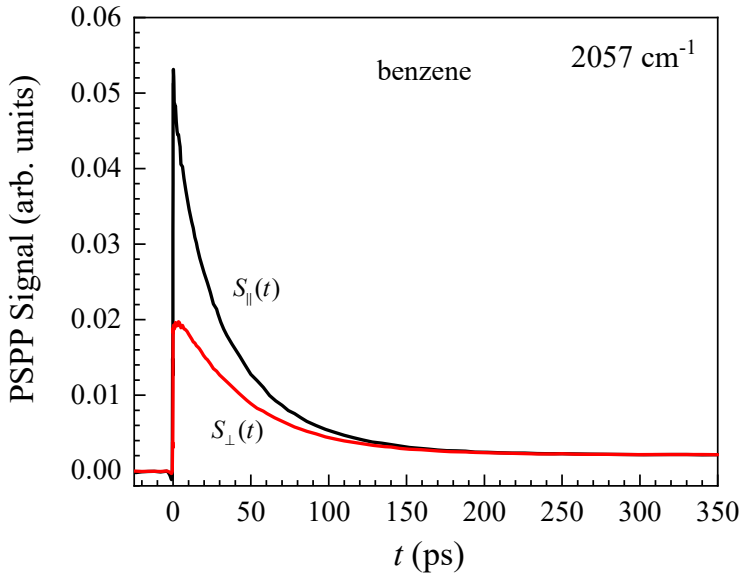

Figure S1. Representative PSPP signals for isolated silanols (Si-OD) in benzene at 2057 cm^{-1}. The offset at long time in both traces is the result of an isotropic heating signal.

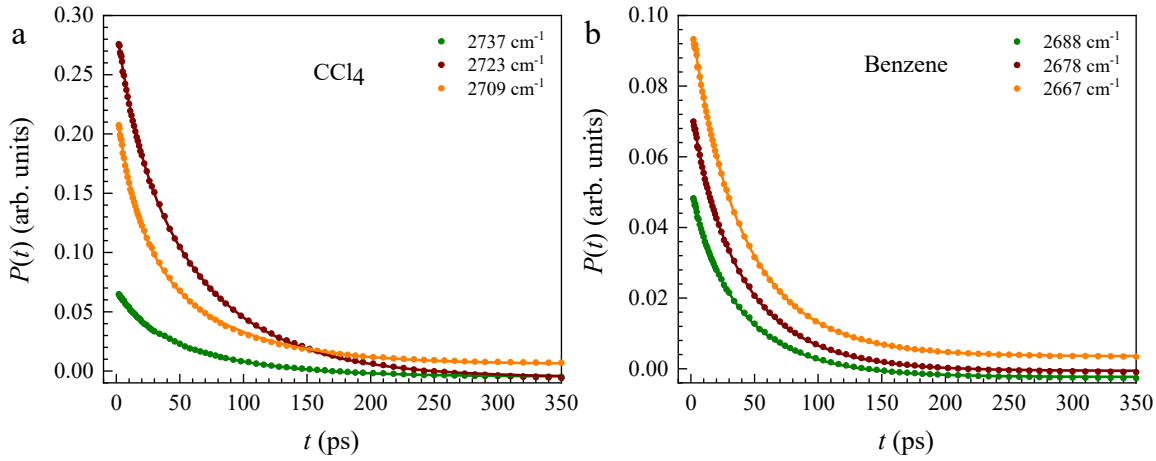

Figure S2. Isotropic pump-probe signals, $P(t)$, with frequency-dependent heating signals evident at long time for isolated silanols (Si-OD) in **(a)** CCl_4 and **(b)** benzene.

When the temperature is increased, the OD absorption band blue-shifts.[18-20] Because the pump-probe signals are obtained by subtracting the signal (probe intensity) when the pump is off from that when the pump is on, this appears as a bleach (positive offset) and induced absorption (negative offset) on the red and blue side of the transient absorption spectrum, respectively (Fig. S2). The temperature increase occurs when the excited vibration relaxes to the ground state and releases its energy to the surrounding solvent. The signal thus grows according to the vibrational lifetime of the relaxing mode. Since the diffusion of heat out of the excited volume occurs on the order of μs to ms, it appears as a static offset within the time-window of the experiment; in this case, 0-350 ps. In most situations, including the present one, the heating signal equally influences $S_{\parallel}(t)$ and $S_{\perp}(t)$ (Fig. S1). In other words, it is isotropic. Anisotropic heating has also been reported, but does not need to be considered here.[21]

Here we assume that the excited vibration directly relaxes into the ground-state. In certain cases an intermediate state has been invoked to better model the kinetics of the heat-signal growth.[18, 19] We found that inclusion of an intermediate state is not necessary in the present case. As discussed in the main text, we observe two types of surface silanols that have distinctly different vibrational lifetimes. Thus, in our model, the heating signal will grow in as a biexponential with time constants equal to the two observed lifetimes. The un-processed $P(t)$ were fit to a function of the following form,

$$f(t) = (A_{\mathrm{II}} + A_{\mathrm{I}})\Gamma + (A_{\mathrm{II}}e^{-t/T_1^{\mathrm{II}}} + A_{\mathrm{I}}e^{-t/T_1^{\mathrm{I}}})(1-\Gamma), \tag{S4}$$

where A_{II} and A_{I} are the amplitudes of the vibrational lifetimes T_1^{II} and T_1^{I}, respectively. This equation is simply equivalent to the sum of a biexponential population decay signal and a biexponential heat growth signal. If the static heating signal observed at long time in the un-processed $P(t)$ decay is denoted H, then from Eq. (S4) the constant $\Gamma = H/(A_{\mathrm{II}} + A_{\mathrm{I}})$. Thus, an implicit assumption of Eq. (S4) is that the contribution of a given lifetime component to the heating signal is proportional to its normalized amplitude in the $P(t)$ decay. In other words, the final heating signal contributions of the T_1^{II} and T_1^{I} components are respectively given by $[A_{\mathrm{II}}/(A_{\mathrm{II}} + A_{\mathrm{I}})]H = a_{\mathrm{II}}H$ and $[A_{\mathrm{I}}/(A_{\mathrm{II}} + A_{\mathrm{I}})]H = a_{\mathrm{I}}H$, with $a_{\mathrm{II}} + a_{\mathrm{I}} = 1$.

In the main text, the expression for $P(t)$ contains a factor of 1/3, in keeping with its conventional definition.[8] However, throughout this analysis we omit the factor of 1/3, and simply use the proportional quantity $P(t) \propto S_{\parallel}(t) + 2S_{\perp}(t) = A_{\mathrm{II}}e^{-t/T_1^{\mathrm{II}}} + A_{\mathrm{I}}e^{-t/T_1^{\mathrm{I}}}$. Subtracting this expression from Eq. (S4) gives the time-dependent heating signal:

$$h(t) = \Gamma\{A_{\mathrm{II}}(1-e^{-t/T_1^{\mathrm{II}}}) + A_{\mathrm{I}}(1-e^{-t/T_1^{\mathrm{I}}})\}. \tag{S5}$$

Therefore, the un-processed $P(t)$ was corrected by subtracting $h(t)$. Since the heating signal is isotropic (Fig. S1), the un-processed $S_{\parallel}(t)$ and $S_{\perp}(t)$ were corrected by subtracting $h(t)/3$ from each signal. Note that the frequency dependence of $P(t)$ and $h(t)$ have been suppressed in the above discussion, but were taken into account in the data processing. The corrected $P(t)$ and $r(t)$ observables are shown in Fig. 2 and Fig. 5, respectively.

B. 2D IR Spectroscopy

The heating signal discussed in the context of the PSPP experiment will also manifest in the 2D IR experiment and distort the 2D band shape. At intermediate time delays, both the resonant signal and heating signal will overlap. At very long delays, the resonant signal contribution will have decayed completely with the vibrational lifetime, leaving only the heating

signal contribution. Representative heating signal 2D IR spectra acquired at T_w = 500 ps for MCM41-OD in CCl_4 and Bz are shown in Fig. S3(a) and S3(b), respectively. This delay time corresponds to ~7 and ~11 factors of the longest vibrational lifetimes in the CCl_4 and Bz samples, respectively. Thus, in the following, these long time spectra are denoted the $T_w = \infty$ spectra. For MCM41-OD in the pure solvents, the heating signal, $S^{heat}(\omega_1, \infty, \omega_3)$, was removed according to,

$$S(\omega_1, T_w, \omega_3) = S^{obs}(\omega_1, T_w, \omega_3) - \frac{h(T_w)}{\Gamma(A_{II} + A_I)} S^{heat}(\omega_1, \infty, \omega_3)$$
$$= S^{obs}(\omega_1, T_w, \omega_3) - [a_{II}(1 - e^{-t/T_1^{II}}) + a_I(1 - e^{-t/T_1^{I}})] S^{heat}(\omega_1, \infty, \omega_3), \quad \text{(S6)}$$

where $S^{obs}(\omega_1, T_w, \omega_3)$ is the observed 2D IR spectrum. In Eq. (S6), a_{II} and a_I corresponding to the center frequencies 2723 cm^{-1} and 2667 cm^{-1} were used for the CCl_4 and Bz samples, respectively.

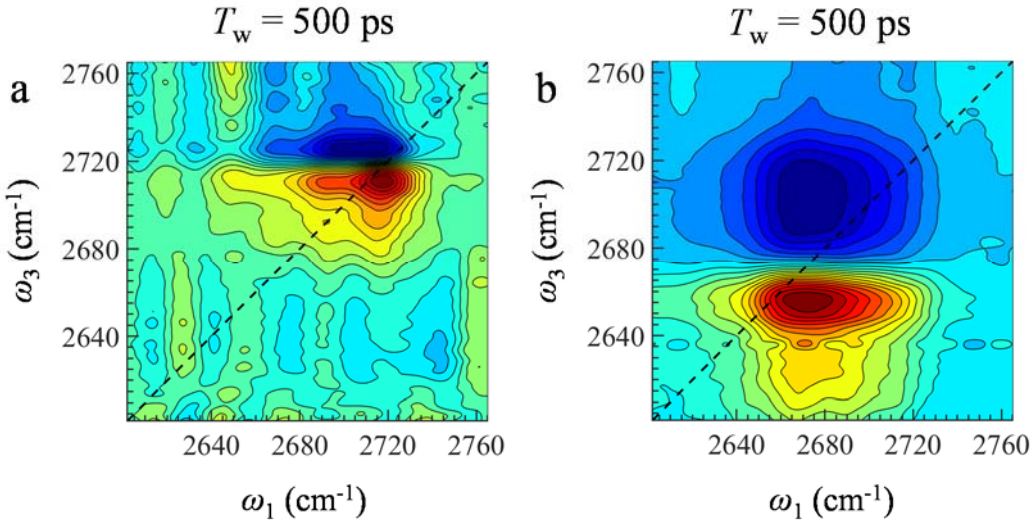

Figure S3. Long time (T_w = 500 ps) heating signal 2D IR spectra for isolated silanols (Si-OD) in **(a)** CCl_4 and **(b)** benzene.

The MCM41-OD mixed solvent 2D IR spectra (1:5 Bz:CCl_4) will also contain a heating signal contribution. The removal of this heating signal is less trivial than in the case of the pure

solvent spectra discussed above. Whereas the 2D band shape of the heating signal in the pure solvents is taken to be time-independent (the amplitude being the only time-dependent quantity), this is not so in the case of the mixed solvent. The reason for this is that the heating signals corresponding to Bz and CCl_4 associated isolated silanols are spectrally distinct and grow in at different rates dictated by the vibrational lifetimes of the OD oscillators in the two environments. To remove heating from the 1:5 Bz:CCl_4 spectra, we must linearly combine the heating signals from the pure Bz and pure CCl_4 spectra and subtract the result from the observed 1:5 Bz:CCl_4 spectra in a T_w dependent manner. This is clearly a first-order approach to removing the heating signal and does not consider higher-order cross-interactions between the two solvents. Even if the laser conditions and MCM41-OD samples were identical, with the only variable being the solvent, one would still have to adjust the amplitudes of the pure solvent heating signals to obtain a reasonable first-order approximation to the heating signal in the 1:5 Bz:CCl_4 sample. This is because the number of silanols associated with Bz and CCl_4 is very different between the mixed solvent sample and the pure solvent samples. Fortunately, the T_w dependence is known from PSPP experiments on the pure solvent samples. The additional information left to be determined is the absolute scale of the Bz and CCl_4 heating spectra and their relative ratio in the sum, which will then be used to subtract the T_w dependent heating from the 1:5 Bz:CCl_4 sample. This will require two additional scalar parameters. Therefore, if we denote the heating signals in the various cases as $S^{\text{heat}}_{CCl_4}(\omega_1,\infty,\omega_3)$, $S^{\text{heat}}_{Bz}(\omega_1,\infty,\omega_3)$, and $S^{\text{heat}}_{Bz/CCl_4}(\omega_1,\infty,\omega_3)$, our approach was to first reconstruct $S^{\text{heat}}_{Bz/CCl_4}(\omega_1,\infty,\omega_3)$ as a linear combination of the pure solvent heating signals,

$$S^{\text{heat}}_{Bz/CCl_4}(\omega_1,\infty,\omega_3) \sim n\cdot S^{\text{heat}}_{CCl_4}(\omega_1,\infty,\omega_3) + m\cdot S^{\text{heat}}_{Bz}(\omega_1,\infty,\omega_3), \tag{S7}$$

where n and m are scalar quantities that were determined using a nonlinear least-square solver in MATLAB R2019a. Fig. S4(a) displays the long time mixed solvent heating 2D IR spectrum, $S^{\text{heat}}_{Bz/CCl_4}(\omega_1,\infty,\omega_3)$. The best fit of Eq. (S7) to this spectrum, using the pure solvent heating spectra from Fig. S3, is shown in Fig. S4(b). It can be seen that the fit overestimates certain positive and negative regions relative to the measured spectrum, but overall the agreement is

adequate for significant removal of this relatively small artifact. The heating signal was subsequently removed from the 2D IR chemical exchange spectra at all T_w values according to,

$$S(\omega_1,T_w,\omega_3) = S^{\text{obs}}(\omega_1,T_w,\omega_3) - \left\{ \frac{n \cdot h_{CCl_4}(T_w)}{\Gamma_{CCl_4}(A_{II}^{CCl_4} + A_I^{CCl_4})} S_{CCl_4}^{\text{heat}}(\omega_1,\infty,\omega_3) + \frac{m \cdot h_{Bz}(T_w)}{\Gamma_{Bz}(A_{II}^{Bz} + A_I^{Bz})} S_{Bz}^{\text{heat}}(\omega_1,\infty,\omega_3) \right\}, \quad \text{(S8)}$$

where the parameters for CCl_4 and Bz appearing in Eq. (S8) corresponding to the frequencies 2717 cm^{-1} and 2670 cm^{-1} were used. These frequencies are the closest to the peak maxima observed in the mixed solvent linear absorption spectrum (see Fig. 1 and Table 1).

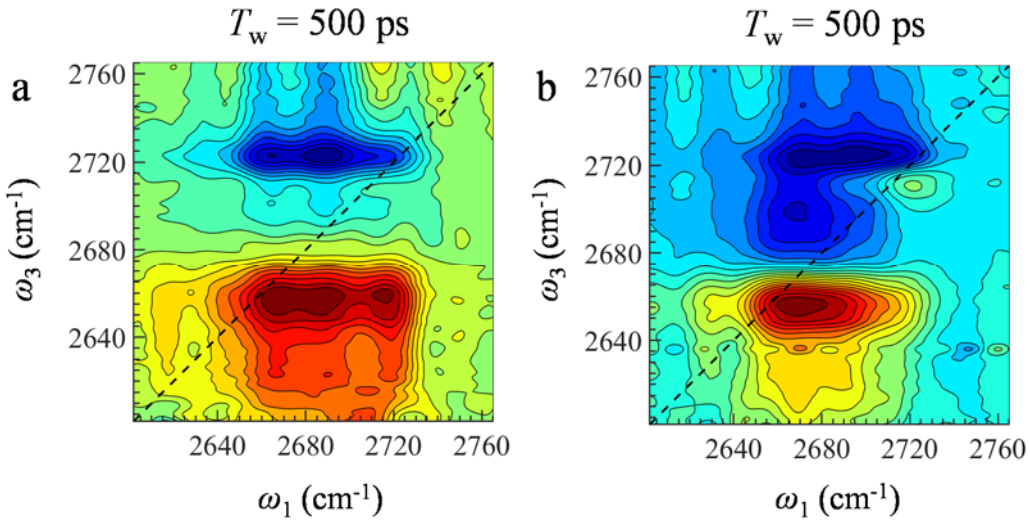

Figure S4. (a) Long time (T_w = 500 ps) heating signal 2D IR spectrum for isolated silanols (Si-OD) in 1:5 Bz:CCl_4. **(b)** Best fit to the spectrum in (a) using a linear combination of the pure solvent heating signal spectra from Fig. S3.

SIII. Chemical Exchange Theory

A. Dynamic Partition Model

The theory of 2D IR chemical exchange experiments was previously presented by Kwak et al.[12] The discussion that follows is for a single population of vibrational oscillators (for example, a single silanol type). A single population in dynamic equilibrium can be divided into

six sub-ensembles that contribute to the observed 2D IR line shapes.[12] At the beginning of the population period, T_w = 0 ps, two diagonal peaks, one originating from the total population of free oscillators, N_f, and the other from the total population of complexed oscillators, N_c, are excited and detected. As the population period increases, chemical exchange proceeds as free oscillators become complexed, N_fc, and vice versa, N_cf. If the diagonal peaks arising from N_f and N_c occur at different frequencies, the populations that have undergone exchange an *odd* number of times during the T_w period, N_fc and N_cf, will give rise to off-diagonal cross-peaks. Population transfer from a diagonal peak to a cross-peak, or the reverse, can only occur along the ω_3 detection axis. This is because peaks exchanging population in the 2D IR spectrum must be excited at the same initial frequency, i.e. the same position along the ω_1 detection axis.

So far, oscillators that exchange an *even* number of times before detection have been neglected in this discussion. Such oscillators will ultimately end up in the same state that they began, either free or complexed. Therefore, the peak corresponding to this population will also show up on the diagonal of the 2D IR spectrum. However, the line shape differs from that of the sub-ensemble that underwent no exchanges, or those that remained on the diagonal for the entire population period (see below).[12] Thus, both time-dependent populations contributing to a diagonal peak must be modeled to accurately describe the 2D line shape. This can be done by first noting that,

$$N_\mathrm{f} = N_\mathrm{f}^\mathrm{s} + N_\mathrm{f}^\mathrm{ex}, \tag{S9}$$

where N_f^s is the population that stayed free for the entire population period (underwent zero exchanges), and N_f^ex is the population that were initially free and exchanged an even number of times. An analogous equation holds for N_c. It will be shown below that both N_f and N_f^s (and N_c and N_c^s) can be independently calculated. Using Eq. (S9), N_f^ex (and N_c^ex) can then be determined. In summary, for a single type of oscillator, the time-dependence of six sub-ensembles must be tracked: N_f^s and N_f^ex (free species diagonal peak), N_c^s and N_c^ex (complexed species diagonal peak), and N_fc and N_cf (cross-peaks).

The contribution of a given oscillator to the vibrational echo signal is determined by several factors including its exchange rate, lifetime, rate of rotation, transition dipole moment magnitude, and the polarization configuration of the echo signal being measured. The relevant kinetic pathways are depicted graphically in Fig. 7 for the perpendicular ($\langle XXYY \rangle$) polarization configuration, where $k_{\mathrm{f}} = 1/T_{1,\mathrm{f}}$ and $k_{\mathrm{c}} = 1/T_{1,\mathrm{c}}$ are the inverse lifetimes of the free and complexed species, respectively, k_{fc} is the rate of complexation, k_{cf} is the rate of dissociation, and $6D_{\mathrm{f}}$ and $6D_{\mathrm{c}}$ are the rates of rotation for the free and complexed species, respectively. For the perpendicular configuration, rotation causes a growth of the echo signal, which is why the arrows point inwards.[22, 23] For the parallel configuration ($\langle XXXX \rangle$), rotation causes a decay of the echo signal,[12, 22, 23] and the only change to Fig. 7 would be outward pointing arrows accompanying each rotation pathway. The vibrational lifetime causes the signal to decay regardless of polarization, so the arrows associated with the vibrational lifetime are always outward pointing.

The influence of polarization on the effective populations requires ensemble averaging over the orientational distribution of the transition dipole moment unit vector, $\hat{\boldsymbol{\mu}}$. The orientation of the unit vector can be specified in spherical coordinates as $\Omega = (\theta, \phi)$. We assume that the probability that $\hat{\boldsymbol{\mu}}$ is oriented in the direction Ω at time t, $P(\Omega, t)$, is governed by the diffusion equation,[12]

$$\frac{\partial}{\partial t} P(\Omega, t) = -DI^2 P(\Omega, t), \tag{S10}$$

where I is the dimensionless orbital angular momentum operator from quantum mechanics.[24] Before performing the ensemble averaging, the populations evolve according to,[12, 22]

$$\frac{d}{dt}\begin{pmatrix} N_{\mathrm{f}}^{*}(t)\cdot P_{\mathrm{f}}(\Omega,t) \\ N_{\mathrm{cf}}^{*}(t)\cdot P_{\mathrm{cf}}(\Omega,t) \\ N_{\mathrm{c}}^{*}(t)\cdot P_{\mathrm{c}}(\Omega,t) \\ N_{\mathrm{fc}}^{*}(t)\cdot P_{\mathrm{fc}}(\Omega,t) \end{pmatrix} = \begin{pmatrix} -(k_{\mathrm{f}}+k_{\mathrm{fc}}+D_{\mathrm{f}}I^2) & 0 & 0 & k_{\mathrm{cf}} \\ 0 & -(k_{\mathrm{f}}+k_{\mathrm{fc}}+D_{\mathrm{f}}I^2) & k_{\mathrm{cf}} & 0 \\ 0 & k_{\mathrm{fc}} & -(k_{\mathrm{c}}+k_{\mathrm{cf}}+D_{\mathrm{c}}I^2) & 0 \\ k_{\mathrm{fc}} & 0 & 0 & -(k_{\mathrm{c}}+k_{\mathrm{cf}}+D_{\mathrm{c}}I^2) \end{pmatrix} \begin{pmatrix} N_{\mathrm{f}}^{*}(t)\cdot P_{\mathrm{f}}(\Omega,t) \\ N_{\mathrm{cf}}^{*}(t)\cdot P_{\mathrm{cf}}(\Omega,t) \\ N_{\mathrm{c}}^{*}(t)\cdot P_{c}(\Omega,t) \\ N_{\mathrm{fc}}^{*}(t)\cdot P_{\mathrm{fc}}(\Omega,t) \end{pmatrix}, \tag{S11}$$

where the superscript asterisks in Eq. (S11) denote the populations before the ensemble average is taken. The solution to Eq. (S11) can be written in matrix form as,

$$\begin{pmatrix} N_{\mathrm{f}}^{*}(t)\cdot P_{\mathrm{f}}(\Omega,t) \\ N_{\mathrm{cf}}^{*}(t)\cdot P_{\mathrm{cf}}(\Omega,t) \\ N_{\mathrm{c}}^{*}(t)\cdot P_{\mathrm{c}}(\Omega,t) \\ N_{\mathrm{fc}}^{*}(t)\cdot P_{\mathrm{fc}}(\Omega,t) \end{pmatrix} = \exp\left[\begin{pmatrix} -(k_{\mathrm{f}}+k_{\mathrm{fc}}+D_{\mathrm{f}}I^2) & 0 & 0 & k_{\mathrm{cf}} \\ 0 & -(k_{\mathrm{f}}+k_{\mathrm{fc}}+D_{\mathrm{f}}I^2) & k_{\mathrm{cf}} & 0 \\ 0 & k_{\mathrm{fc}} & -(k_{\mathrm{c}}+k_{\mathrm{cf}}+D_{\mathrm{c}}I^2) & 0 \\ k_{\mathrm{fc}} & 0 & 0 & -(k_{\mathrm{c}}+k_{\mathrm{cf}}+D_{\mathrm{c}}I^2) \end{pmatrix} t\right] \begin{pmatrix} N_{\mathrm{f}}^{*}(0)\cdot P_{\mathrm{f}}(\Omega,0) \\ N_{\mathrm{cf}}^{*}(0)\cdot P_{\mathrm{cf}}(\Omega,0) \\ N_{\mathrm{c}}^{*}(0)\cdot P_{c}(\Omega,0) \\ N_{\mathrm{fc}}^{*}(0)\cdot P_{\mathrm{fc}}(\Omega,0) \end{pmatrix}. \tag{S12}$$

For the parallel and perpendicular polarization configurations, $\langle XXXX\rangle = \langle ZZZZ\rangle$ and $\langle XXYY\rangle = \langle ZZYY\rangle$, the initial angular distribution functions are respectively,

$$\begin{aligned} P_i^{ZZZZ}(\Omega,0) &= \frac{3}{4\pi}\cos^2\theta \\ &= \sqrt{\frac{1}{4\pi}}Y_0^0(\Omega)+\sqrt{\frac{1}{5\pi}}Y_2^0(\Omega), \end{aligned} \tag{S13}$$

and

$$\begin{aligned} P_i^{ZZYY}(\Omega,0) &= \frac{3}{4\pi}(\sin\theta\sin\phi)^2 \\ &= \sqrt{\frac{1}{4\pi}}Y_0^0(\Omega)-\frac{3}{2\sqrt{2}}\sqrt{\frac{1}{15\pi}}(Y_2^2(\Omega)+Y_2^{-2}(\Omega))-\frac{1}{2}\sqrt{\frac{1}{5\pi}}Y_2^0(\Omega), \end{aligned} \tag{S14}$$

where the distributions have been expanded in the spherical harmonics. The ensemble average in either case is given by,

$$\langle ... \rangle \equiv \int d\Omega [...] \cos^2 \theta, \tag{S15}$$

where $\int d\Omega = \int_0^{2\pi} d\phi \int_0^{\pi} d\theta \sin\theta$. After substituting the initial conditions, Eqs. (S13) and (S14), into Eq. (S12), and using the fact that the spherical harmonics are eigenfunctions of I^2, or $I^2 Y_l^m(\Omega) = l(l+1) Y_l^m(\Omega)$ for $l = 0, 1, 2, \ldots$, the intermediate results for parallel and perpendicular are, respectively,

$$\begin{pmatrix} N_{\mathrm{f}}^*(t) \cdot P_{\mathrm{f}}(\Omega, t) \\ N_{\mathrm{cf}}^*(t) \cdot P_{\mathrm{cf}}(\Omega, t) \\ N_{\mathrm{c}}^*(t) \cdot P_{\mathrm{c}}(\Omega, t) \\ N_{\mathrm{fc}}^*(t) \cdot P_{\mathrm{fc}}(\Omega, t) \end{pmatrix} = \exp[\mathbf{A}t] \begin{pmatrix} N_{\mathrm{f}}^*(0) \\ N_{\mathrm{cf}}^*(0) \\ N_{\mathrm{c}}^*(0) \\ N_{\mathrm{fc}}^*(0) \end{pmatrix} \left(\sqrt{\frac{1}{4\pi}} Y_0^0(\Omega) \right) + \exp[\mathbf{B}t] \begin{pmatrix} N_{\mathrm{f}}^*(0) \\ N_{\mathrm{cf}}^*(0) \\ N_{\mathrm{c}}^*(0) \\ N_{\mathrm{fc}}^*(0) \end{pmatrix} \left(\sqrt{\frac{1}{5\pi}} Y_2^0(\Omega) \right), \tag{S16}$$

and

$$\begin{aligned} \begin{pmatrix} N_{\mathrm{f}}^*(t) \cdot P_{\mathrm{f}}(\Omega, t) \\ N_{\mathrm{cf}}^*(t) \cdot P_{\mathrm{cf}}(\Omega, t) \\ N_{\mathrm{c}}^*(t) \cdot P_{\mathrm{c}}(\Omega, t) \\ N_{\mathrm{fc}}^*(t) \cdot P_{\mathrm{fc}}(\Omega, t) \end{pmatrix} = \exp[\mathbf{A}t] \begin{pmatrix} N_{\mathrm{f}}^*(0) \\ N_{\mathrm{cf}}^*(0) \\ N_{\mathrm{c}}^*(0) \\ N_{\mathrm{fc}}^*(0) \end{pmatrix} \left(\sqrt{\frac{1}{4\pi}} Y_0^0(\Omega) \right) + \\ \exp[\mathbf{B}t] \begin{pmatrix} N_{\mathrm{f}}^*(0) \\ N_{\mathrm{cf}}^*(0) \\ N_{\mathrm{c}}^*(0) \\ N_{\mathrm{fc}}^*(0) \end{pmatrix} \left(-\frac{3}{2\sqrt{2}} \sqrt{\frac{1}{15\pi}} (Y_2^2(\Omega) + Y_2^{-2}(\Omega)) - \frac{1}{2} \sqrt{\frac{1}{5\pi}} Y_2^0(\Omega) \right), \end{aligned} \tag{S17}$$

where the matrices $\mathbf{A}$ and $\mathbf{B}$ are given by,

$$\mathbf{A} = \begin{pmatrix} -a_{\text{iso}} & 0 & 0 & d \\ 0 & -a_{\text{iso}} & d & 0 \\ 0 & c & -b_{\text{iso}} & 0 \\ c & 0 & 0 & -b_{\text{iso}} \end{pmatrix}, \tag{S18}$$

and

$$\mathbf{B} = \begin{pmatrix} -a & 0 & 0 & d \\ 0 & -a & d & 0 \\ 0 & c & -b & 0 \\ c & 0 & 0 & -b \end{pmatrix}, \tag{S19}$$

with $a = k_{\text{f}} + k_{\text{fc}} + 6D_{\text{f}}$, $b = k_{\text{c}} + k_{\text{cf}} + 6D_{\text{c}}$, $c = k_{\text{fc}}$, $d = k_{\text{cf}}$, $a_{\text{iso}} = a - 6D_{\text{f}}$, and $b_{\text{iso}} = b - 6D_{\text{c}}$. All of the anisotropic dynamics are contained in the $\mathbf{B}$ matrix, while the isotropic dynamics are contained in the $\mathbf{A}$ matrix, which is independent of the rotational diffusion coefficients. Finally, performing the ensemble average, Eq. (S15), on both sides of Eqs. (S16) and (S17) gives,

$$\frac{9}{15}\begin{pmatrix} N_{\text{f}}(t) \\ N_{\text{cf}}(t) \\ N_{\text{c}}(t) \\ N_{\text{fc}}(t) \end{pmatrix} \equiv \begin{pmatrix} \langle N_{\text{f}}^{*}(t) \cdot P_{\text{f}}(\Omega, t) \rangle \\ \langle N_{\text{cf}}^{*}(t) \cdot P_{\text{cf}}(\Omega, t) \rangle \\ \langle N_{\text{c}}^{*}(t) \cdot P_{\text{c}}(\Omega, t) \rangle \\ \langle N_{\text{fc}}^{*}(t) \cdot P_{\text{fc}}(\Omega, t) \rangle \end{pmatrix} = \frac{1}{3}\left(\exp[\mathbf{A}t] + \frac{4}{5}\exp[\mathbf{B}t] \right) \begin{pmatrix} N_{\text{f}}(0) \\ N_{\text{cf}}(0) \\ N_{\text{c}}(0) \\ N_{\text{fc}}(0) \end{pmatrix} \tag{S20}$$

and

$$\frac{3}{15}\begin{pmatrix} N_{\text{f}}(t) \\ N_{\text{cf}}(t) \\ N_{\text{c}}(t) \\ N_{\text{fc}}(t) \end{pmatrix} \equiv \begin{pmatrix} \langle N_{\text{f}}^{*}(t) \cdot P_{\text{f}}(\Omega, t) \rangle \\ \langle N_{\text{cf}}^{*}(t) \cdot P_{\text{cf}}(\Omega, t) \rangle \\ \langle N_{\text{c}}^{*}(t) \cdot P_{\text{c}}(\Omega, t) \rangle \\ \langle N_{\text{fc}}^{*}(t) \cdot P_{\text{fc}}(\Omega, t) \rangle \end{pmatrix} = \frac{1}{3}\left(\exp[\mathbf{A}t] - \frac{2}{5}\exp[\mathbf{B}t] \right) \begin{pmatrix} N_{\text{f}}(0) \\ N_{\text{cf}}(0) \\ N_{\text{c}}(0) \\ N_{\text{fc}}(0) \end{pmatrix} \tag{S21}$$

for parallel and perpendicular, respectively. For 2D IR chemical exchange experiments, we also have the initial condition: $N_{\mathrm{cf}}(0) = N_{\mathrm{fc}}(0) = 0$. With this initial condition, the solutions can be expressed,

$$\begin{aligned} N_{\mathrm{f}}(t) = N_{\mathrm{f}}(0)\Big\{ & \kappa\left(\lambda_1 - \lambda_2\right)^{-1}\left[e^{\lambda_2 t}(a+\lambda_1) - e^{\lambda_1 t}(a+\lambda_2)\right] \\ & +\eta\left(\lambda_3 - \lambda_4\right)^{-1}\left[e^{\lambda_4 t}(a_{\mathrm{iso}}+\lambda_3) - e^{\lambda_3 t}(a_{\mathrm{iso}}+\lambda_4)\right]\Big\}, \end{aligned} \tag{S22}$$

$$N_{\mathrm{cf}}(t) = N_{\mathrm{c}}(0)d\left\{\kappa\left(\lambda_1 - \lambda_2\right)^{-1}\left[e^{\lambda_1 t} - e^{\lambda_2 t}\right] + \eta\left(\lambda_3 - \lambda_4\right)^{-1}\left[e^{\lambda_3 t} - e^{\lambda_4 t}\right]\right\}, \tag{S23}$$

$$\begin{aligned} N_{\mathrm{c}}(t) = N_{\mathrm{c}}(0)\Big\{ & \kappa\left(\lambda_1 - \lambda_2\right)^{-1}\left[e^{\lambda_2 t}(b+\lambda_1) - e^{\lambda_1 t}(b+\lambda_2)\right] \\ & +\eta\left(\lambda_3 - \lambda_4\right)^{-1}\left[e^{\lambda_4 t}(b_{\mathrm{iso}}+\lambda_3) - e^{\lambda_3 t}(b_{\mathrm{iso}}+\lambda_4)\right]\Big\}, \end{aligned} \tag{S24}$$

$$N_{\mathrm{fc}}(t) = N_{\mathrm{f}}(0)c\left\{\kappa\left(\lambda_1 - \lambda_2\right)^{-1}\left[e^{\lambda_1 t} - e^{\lambda_2 t}\right] + \eta\left(\lambda_3 - \lambda_4\right)^{-1}\left[e^{\lambda_3 t} - e^{\lambda_4 t}\right]\right\}, \tag{S25}$$

with

$$\lambda_1 = 0.5\left\{\left[(a+b)^2 - 4(ab-cd)\right]^{1/2} - (a+b)\right\}, \tag{S26}$$

$$\lambda_2 = -0.5\left\{\left[(a+b)^2 - 4(ab-cd)\right]^{1/2} + (a+b)\right\}, \tag{S27}$$

$$\lambda_3 = 0.5\left\{\left[(a_{\mathrm{iso}}+b_{\mathrm{iso}})^2 - 4(a_{\mathrm{iso}}b_{\mathrm{iso}}-cd)\right]^{1/2} - (a_{\mathrm{iso}}+b_{\mathrm{iso}})\right\}, \tag{S28}$$

$$\lambda_4 = -0.5\left\{\left[(a_{\mathrm{iso}}+b_{\mathrm{iso}})^2 - 4(a_{\mathrm{iso}}b_{\mathrm{iso}}-cd)\right]^{1/2} + (a_{\mathrm{iso}}+b_{\mathrm{iso}})\right\}. \tag{S29}$$

For parallel, κ = 4/9 and η = 5/9, while for perpendicular κ = -2/3 and η = 5/3. If the system is in thermal equilibrium, then the additional relationship also applies,

$$K_{\mathrm{eq}} = \frac{N_{\mathrm{c}}(t)}{N_{\mathrm{f}}(t)} = \frac{k_{\mathrm{fc}}}{k_{\mathrm{cf}}} = \frac{c}{d}, \tag{S30}$$

which means that,

$$N_{\mathrm{c}}(0)d = N_{\mathrm{f}}(0)c. \tag{S31}$$

Consequently, in thermal equilibrium and for a fixed polarization configuration, $N_{\mathrm{cf}}(t) = N_{\mathrm{fc}}(t)$, as can be seen by Eqs. (S23) and (S25). This means that the two populations giving rise to off-diagonal peaks will grow in with the same time-dependence.

As mentioned above, oscillators that exchange an *even* number of times must be distinguished from those that do not exchange. The number of free oscillators that do not undergo exchange, $N_{\mathrm{f}}^{\mathrm{s}}$, can be determined by setting the dissociation rate constant, k_{cf}, to zero. Thus, once an oscillator exchanges from the free to complexed state, it cannot dissociate, or return back to the free state. The population $N_{\mathrm{f}}^{\mathrm{s}}(t)$ is equivalent to the solution to $N_{\mathrm{f}}(t)$ with the added condition $k_{\mathrm{cf}} = 0$, or

$$N_{\mathrm{f}}^{\mathrm{s}}(t) = N_{\mathrm{f}}(t; k_{\mathrm{cf}} = 0). \tag{S32}$$

Substituting Eq. (S32) into Eq. (S9) and rearranging gives,

$$N_{\mathrm{f}}^{\mathrm{ex}}(t) = N_{\mathrm{f}}(t) - N_{\mathrm{f}}(t; k_{\mathrm{cf}} = 0), \tag{S33}$$

which is the population of oscillators that began free and exchanged an even number of times. Analogous equations can be written for the complexed oscillators, but in this case the complexation rate constant, k_{fc}, is set to zero.

-

B. Dynamic Partition Model with Restricted Rotational Diffusion

In the above section, we assumed that the transition dipole moment unit vector for each type of oscillator was undergoing free orientational diffusion with no boundary condition constraining the spatial extent of the motion. However, this assumption is not always accurate, as in the present situation where it is clear that the surface silanols are wobbling over a limited volume of space. Therefore, the boundary condition that limits the rotational motion to a portion of the unit sphere must be incorporated into the kinetic model. To do this, we take the approach of Ji et al. by using an effective time-dependent diffusion coefficient, $D_\alpha(t)$ (where α = c or f),[23]

$$\frac{d}{dt}C_{2,\alpha}(t) = -6D_\alpha(t)C_{2,\alpha}(t), \tag{S34}$$

$$6D_\alpha(t) = -\frac{\ln C_{2,\alpha}(t)}{t}. \tag{S35}$$

In this case, $C_{2,\alpha}(t)$ is the wobbling-in-a-cone orientational correlation function for the α state. This approximation will only change the anisotropic $\mathbf{B}$ matrix in the preceding discussion. The modification is very simple; each factor of $6D_\alpha$ occurring in $\mathbf{B}$ is replaced by $6D_\alpha(t)$.

C. 3rd-order Response Functions for Chemical Exchange

Although the peaks from oscillators that do not exchange and those that exchange an even number of times are centered at the same position along the diagonal, their line shapes are not equivalent. The reason for this is that the two types of oscillators proceed through different quantum pathways.[12] Oscillators that do not exchange, $N_{\mathrm{f}}^{\mathrm{s}}$ and $N_{\mathrm{c}}^{\mathrm{s}}$, will undergo spectral diffusion.[12] The time-dependent band shape is determined by the frequency-frequency correlation function (FFCF) for the vibrational mode.[2, 11, 12, 14, 15] Here we adopt the usual assumption that chemical exchange destroys all frequency correlation.[12] This means that the probability that an oscillator occupies a given frequency in the new state following exchange is determined by the spectral line of the new state. The frequency of the oscillator in its former state has no influence on its frequency in the new state. The assumption of no frequency correlation

following exchange means that, $\langle \delta\omega_c(t)\delta\omega_f(0)\rangle = \langle \delta\omega_f(t)\delta\omega_c(0)\rangle = 0$, where the frequency fluctuation, $\delta\omega(t)$, is the difference between the instantaneous and average frequency, $\delta\omega(t) = \omega(t) - \langle\omega\rangle$. Under this assumption, the diagonal peaks for the populations, N_f^{ex} and N_c^{ex}, exhibit completely de-correlated 2D band shapes that are determined by the product of the linear absorption spectrum of that particular species along the ω_1 and ω_3 axes.[12] For the same reason, the cross-peaks arising from N_{cf} and N_{fc} will be completely de-correlated, but the 2D band shapes will be determined by the product of the linear absorption spectrum of the initial species along ω_1 with that of the final species along ω_3.[25]

Kwak et al. presented the double-sided Feynman diagrams, and corresponding time-domain response functions, relevant to 2D IR chemical exchange experiments.[12] These can be divided into three sets; the general characteristics of the peaks for each set were described qualitatively in the previous paragraph. Each contains rephasing and non-rephasing diagrams for stimulated emission, ground-state bleach, and excited-state absorption Liouville space pathways for a three-level system.[2, 10, 12] The three sets of six response functions apply to 1) the portion of the diagonal peaks arising from oscillators that do not exchange (N_f^s and N_c^s) 2) the portion of the diagonal peaks arising from oscillators that undergo an *even* number of exchanges (N_f^{ex} and N_c^{ex}), and 3) the cross-peaks (off-diagonal) that arise from oscillators that undergo an *odd* number of exchanges (N_{cf} and N_{fc}). The influence of the transition dipole moment magnitude on the strength of the observed signals is contained in the response function expressions. The 0-1 and 1-2 transitions for the diagonal peaks will scale as $|\mu_{\alpha,01}|^4$ and $-|\mu_{\alpha,01}|^2|\mu_{\alpha,12}|^2$, respectively, where the subscript α = c or f. This is identical to the case of a single oscillator in a system with no exchange. However, the 0-1 and 1-2 transitions for the cross-peaks will scale as $|\mu_{\alpha,01}|^2|\mu_{\beta,01}|^2$ and $-|\mu_{\alpha,01}|^2|\mu_{\beta,12}|^2$, respectively, where α and β stand for two different species, c or f.

SIV. Pure Solvent 2D IR Spectra and CLS

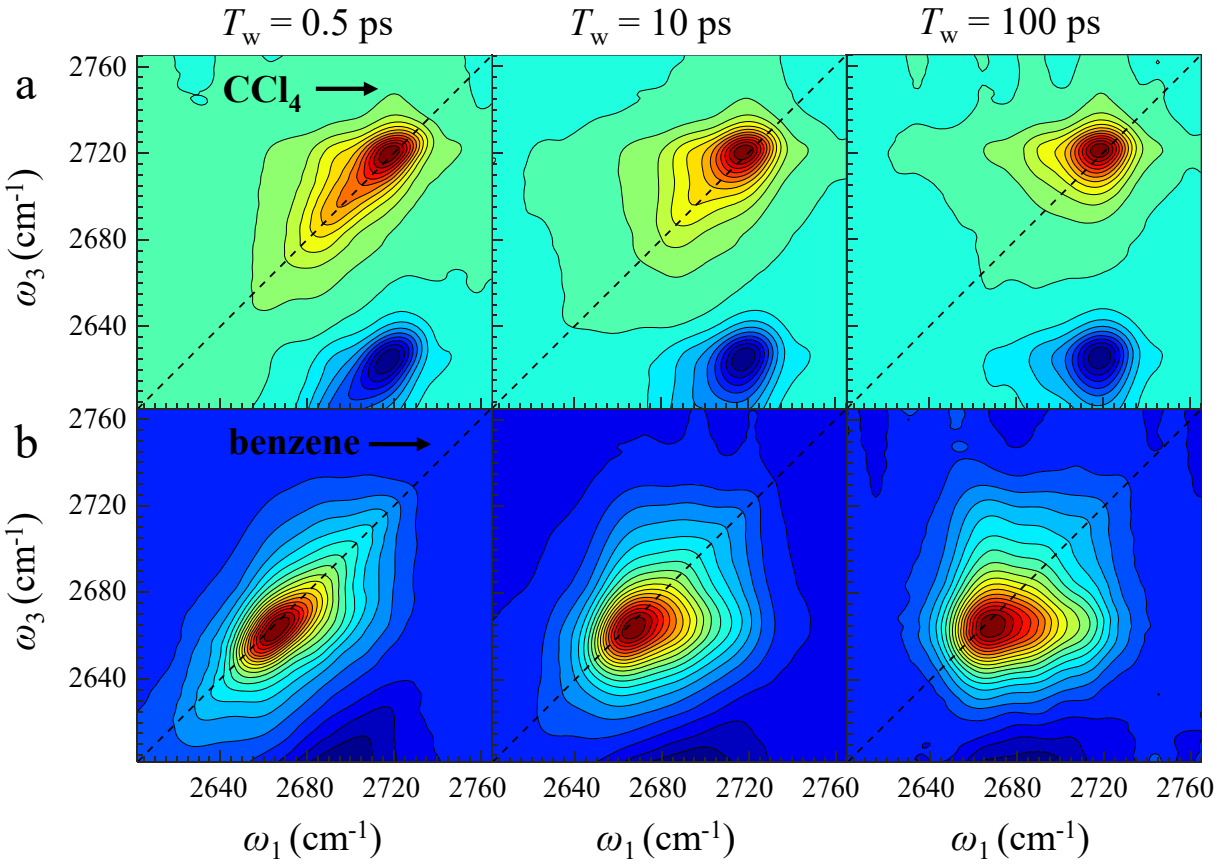

Figure S5. 2D IR spectra in the isolated Si-OD stretching region for silanols in **(a)** CCl_4 and **(b)** benzene at T_w = 0.5 ps, 10 ps, and 100 ps.

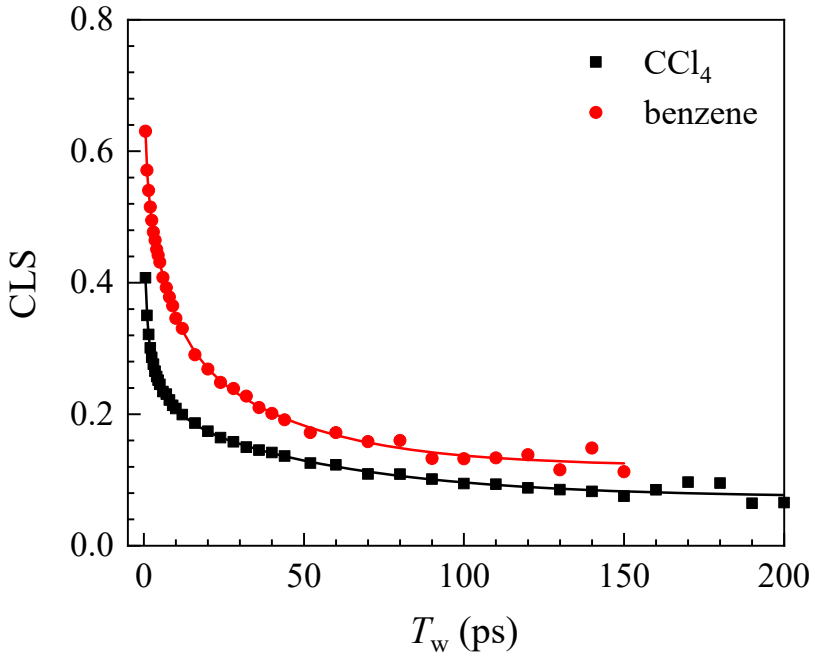

Figure S6. CLS decays for isolated silanols in CCl_4 (black squares) and benzene (red circles). The curves are triexponential fits with an offset.

Table S1. Biexponential fit parameters to $P(t)$ for MCM41-OD in pure CCl4.

frequency (cm^{-1})	A_{II}	T_1^{II} (ps)	A_I	T_1^{I} (ps)
2768	0.0027 ± 0.0003	17.8 ± 0.8	0.010 ± 0.001	71 ± 2
2765	0.0028 ± 0.0003	17.8 ± 0.8	0.010 ± 0.001	71 ± 2
2762	0.0036 ± 0.0005	17.8 ± 0.8	0.011 ± 0.001	71 ± 2
2760	0.0039 ± 0.0005	17.8 ± 0.8	0.012 ± 0.001	71 ± 2
2756	0.0043 ± 0.0007	17.8 ± 0.8	0.014 ± 0.001	71 ± 2
2753	0.0047 ± 0.0007	17.8 ± 0.8	0.016 ± 0.002	71 ± 2
2751	0.005 ± 0.001	17.8 ± 0.8	0.020 ± 0.002	71 ± 2
2748	0.006 ± 0.001	17.8 ± 0.8	0.020 ± 0.001	71 ± 2
2745	0.0076 ± 0.0008	17.8 ± 0.8	0.025 ± 0.001	71 ± 2
2742	0.009 ± 0.001	17.8 ± 0.8	0.031 ± 0.002	71 ± 2
2739	0.010 ± 0.001	17.8 ± 0.8	0.040 ± 0.002	71 ± 2
2737	0.013 ± 0.002	17.8 ± 0.8	0.056 ± 0.003	71 ± 2
2734	0.016 ± 0.002	17.8 ± 0.8	0.078 ± 0.004	71 ± 2
2731	0.022± 0.004	17.8 ± 0.8	0.114 ± 0.007	71 ± 2
2728	0.033 ± 0.005	17.8 ± 0.8	0.16 ± 0.01	71 ± 2
2725	0.045 ± 0.007	17.8 ± 0.8	0.21 ± 0.01	71 ± 2
2723	0.061 ± 0.008	17.8 ± 0.8	0.24 ± 0.02	71 ± 2
2720	0.073 ± 0.009	17.8 ± 0.8	0.24 ± 0.02	71 ± 2
2717	0.081 ± 0.008	17.8 ± 0.8	0.22 ± 0.02	71 ± 2
2714	0.087 ± 0.007	17.8 ± 0.8	0.19 ± 0.02	71 ± 2
2712	0.093 ± 0.007	17.8 ± 0.8	0.16 ± 0.01	71 ± 2
2709	0.098 ± 0.007	17.8 ± 0.8	0.13 ± 0.01	71 ± 2
2706	0.104 ± 0.006	17.8 ± 0.8	0.11 ± 0.01	71 ± 2
2704	0.109 ± 0.006	17.8 ± 0.8	0.091 ± 0.009	71 ± 2
2701	0.112 ± 0.007	17.8 ± 0.8	0.076 ± 0.008	71 ± 2
2698	0.114 ± 0.006	17.8 ± 0.8	0.063 ± 0.007	71 ± 2
2696	0.113 ± 0.006	17.8 ± 0.8	0.053 ± 0.006	71 ± 2
2693	0.110 ± 0.006	17.8 ± 0.8	0.045 ± 0.005	71 ± 2
2690	0.107 ± 0.005	17.8 ± 0.8	0.039 ± 0.005	71 ± 2
2688	0.099 ± 0.005	17.8 ± 0.8	0.032 ± 0.005	71 ± 2
2685	0.091 ± 0.004	17.8 ± 0.8	0.028 ± 0.004	71 ± 2
2683	0.082 ± 0.003	17.8 ± 0.8	0.023 ± 0.004	71 ± 2

Table S2. Biexponential fit parameters to $P(t)$ for MCM41-OD in pure benzene.

frequency (cm^{-1})	A_{II}	T_1^{II} (ps)	A_I	T_1^{I} (ps)
2707	0.0062 ± 0.0004	15 ± 1	0.025 ± 0.003	46.7 ± 0.6
2705	0.0065 ± 0.0004	15 ± 1	0.027 ± 0.004	46.7 ± 0.6
2702	0.0073 ± 0.0007	15 ± 1	0.028 ± 0.004	46.7 ± 0.6
2699	0.0083 ± 0.0007	15 ± 1	0.030 ± 0.004	46.7 ± 0.6
2696	0.0088 ± 0.0007	15 ± 1	0.032 ± 0.004	46.7 ± 0.6
2694	0.0091 ± 0.0009	15 ± 1	0.034 ± 0.004	46.7 ± 0.6
2691	0.0099 ± 0.0009	15 ± 1	0.037 ± 0.005	46.7 ± 0.6
2688	0.011 ± 0.001	15 ± 1	0.040 ± 0.005	46.7 ± 0.6
2686	0.011 ± 0.001	15 ± 1	0.044 ± 0.005	46.7 ± 0.6
2683	0.012 ± 0.002	15 ± 1	0.049 ± 0.006	46.7 ± 0.6
2680	0.012 ± 0.002	15 ± 1	0.053 ± 0.006	46.7 ± 0.6
2678	0.013 ± 0.002	15 ± 1	0.061 ± 0.007	46.7 ± 0.6
2675	0.014 ± 0.002	15 ± 1	0.067 ± 0.007	46.7 ± 0.6
2673	0.014 ± 0.002	15 ± 1	0.074 ± 0.008	46.7 ± 0.6
2670	0.015 ± 0.002	15 ± 1	0.079 ± 0.008	46.7 ± 0.6
2667	0.015 ± 0.003	15 ± 1	0.083 ± 0.009	46.7 ± 0.6
2665	0.015 ± 0.003	15 ± 1	0.086 ± 0.009	46.7 ± 0.6
2662	0.015 ± 0.002	15 ± 1	0.084 ± 0.009	46.7 ± 0.6
2660	0.015 ± 0.003	15 ± 1	0.081 ± 0.009	46.7 ± 0.6
2657	0.015 ± 0.003	15 ± 1	0.075 ± 0.008	46.7 ± 0.6
2654	0.015 ± 0.003	15 ± 1	0.068 ± 0.008	46.7 ± 0.6
2652	0.016 ± 0.002	15 ± 1	0.059 ± 0.007	46.7 ± 0.6
2649	0.016 ± 0.003	15 ± 1	0.052 ± 0.006	46.7 ± 0.6
2647	0.016 ± 0.002	15 ± 1	0.044 ± 0.006	46.7 ± 0.6

Table S3. Two-component fit parameters to $r(t)$ for MCM41-OD in pure CCl_4.

freq. (cm^{-1})	a_{II}	T_1^{II} (ps)	θ_{in}^{II} (°)	θ_{c1}^{II} (°)	τ_{c1}^{II} (ps)	T_1^{I} (ps)	θ_{in}^{I} (°)	θ_{c1}^{I} (°)	τ_{c1}^{I} (ps)
2745	0.23 ± 0.03	17.8 ± 0.8	30 ± 6	40 ± 29	6.5 ± 0.2	71 ± 2	30 ± 5	46 ± 3	1.0 ± 0.1
2742	0.22 ± 0.03	17.8 ± 0.8	27 ± 5	34 ± 27	6.5 ± 0.2	71 ± 2	31 ± 2	44 ± 3	1.0 ± 0.1
2739	0.21 ± 0.03	17.8 ± 0.8	25 ± 3	32 ± 16	6.5 ± 0.2	71 ± 2	32 ± 1	42 ± 2	1.0 ± 0.1
2737	0.18 ± 0.02	17.8 ± 0.8	14 ± 7	28 ± 14	6.5 ± 0.2	71 ± 2	34 ± 1	39 ± 2	1.0 ± 0.1
2734	0.17 ± 0.03	17.8 ± 0.8	0 ± 5	23 ± 11	6.5 ± 0.2	71 ± 2	33 ± 1	39 ± 1	1.0 ± 0.1
2731	0.16 ± 0.03	17.8 ± 0.8	0 ± 3	0 ± 10	6.5 ± 0.2	71 ± 2	31.6 ± 0.4	39 ± 2	1.0 ± 0.1
2728	0.17 ± 0.02	17.8 ± 0.8	0 ± 0	6 ± 9	6.5 ± 0.2	71 ± 2	30.8 ± 0.8	38 ± 1	1.0 ± 0.1
2725	0.18 ± 0.03	17.8 ± 0.8	0 ± 0	6 ± 9	6.5 ± 0.2	71 ± 2	29.5 ± 0.1	38 ± 1	1.0 ± 0.1
2723	0.21 ± 0.02	17.8 ± 0.8	0 ± 0	10 ± 8	6.5 ± 0.2	71 ± 2	28.6 ± 0.5	39 ± 1	1.0 ± 0.1
2720	0.24 ± 0.02	17.8 ± 0.8	0 ± 0	16 ± 8	6.5 ± 0.2	71 ± 2	28.0 ± 0.5	39 ± 2	1.0 ± 0.1
2717	0.27 ± 0.02	17.8 ± 0.8	0 ± 0	20 ± 5	6.5 ± 0.2	71 ± 2	27.2 ± 0.5	41 ± 2	1.0 ± 0.1
2714	0.32 ± 0.01	17.8 ± 0.8	0 ± 0	22 ± 4	6.5 ± 0.2	71 ± 2	26.2 ± 0.6	42 ± 2	1.0 ± 0.1
2712	0.37 ± 0.01	17.8 ± 0.8	0 ± 0	26 ± 3	6.5 ± 0.2	71 ± 2	26.8 ± 0.2	43 ± 2	1.0 ± 0.1
2709	0.42 ± 0.01	17.8 ± 0.8	9 ± 1	27 ± 2	6.5 ± 0.2	71 ± 2	24.4 ± 0.8	45 ± 2	1.0 ± 0.1
2706	0.48 ± 0.01	17.8 ± 0.8	13 ± 1	28 ± 2	6.5 ± 0.2	71 ± 2	23.2 ± 0.9	46 ± 2	1.0 ± 0.1
2704	0.54 ± 0.01	17.8 ± 0.8	16 ± 1	29 ± 2	6.5 ± 0.2	71 ± 2	19.8 ± 0.7	47 ± 2	1.0 ± 0.1
2701	0.60 ± 0.01	17.8 ± 0.8	18 ± 1	29 ± 1	6.5 ± 0.2	71 ± 2	17 ± 1	48 ± 2	1.0 ± 0.1
2698	0.64 ± 0.01	17.8 ± 0.8	19 ± 2	28 ± 2	6.5 ± 0.2	71 ± 2	11 ± 4	50 ± 3	1.0 ± 0.1
2696	0.68 ± 0.01	17.8 ± 0.8	19 ± 1	30 ± 1	6.5 ± 0.2	71 ± 2	8 ± 2	50 ± 3	1.0 ± 0.1
2693	0.71 ± 0.01	17.8 ± 0.8	19 ± 2	30 ± 1	6.5 ± 0.2	71 ± 2	0 ± 5	50 ± 3	1.0 ± 0.1
2690	0.73 ± 0.02	17.8 ± 0.8	18 ± 2	31 ± 1	6.5 ± 0.2	71 ± 2	0 ± 4	49 ± 3	1.0 ± 0.1

Table S4. Single-component fit parameters to $r(t)$ for MCM41-OD in pure benzene.

freq. (cm^{-1})	θ_{in1} (°)	θ_{c1} (°)	θ_{c2} (°)	τ_{c1} (ps)	τ_{c2} (ps)
2707	24.1 ± 0.4	31.0 ± 0.6	40.8 ± 0.8	4.4 ± 0.1	50 ± 1
2705	24.1 ± 0.4	30.3 ± 0.6	42.0 ± 0.7		
2702	22.9 ± 0.4	31.0 ± 0.6	42.4 ± 0.7		
2699	22.8 ± 0.4	30.0 ± 0.6	45.4 ± 0.7		
2696	22.1 ± 0.5	29.7 ± 0.6	46.3 ± 0.7		
2694	21.6 ± 0.5	29.9 ± 0.6	45.1 ± 0.7		
2691	20.5 ± 0.5	30.1 ± 0.6	42.6 ± 0.7		
2688	20.0 ± 0.5	29.4 ± 0.6	47.5 ± 0.7		
2686	19.4 ± 0.5	29.2 ± 0.6	46.9 ± 0.7		
2683	18.2 ± 0.5	29.7 ± 0.6	45.8 ± 0.7		
2680	17.8 ± 0.5	28.7 ± 0.6	47.6 ± 0.7		
2678	16.4 ± 0.6	28.9 ± 0.6	46.9 ± 0.7		
2675	15.7 ± 0.6	28.3 ± 0.6	48.3 ± 0.7		
2673	14.8 ± 0.6	28.0 ± 0.6	47.0 ± 0.6		
2670	13.9 ± 0.6	27.9 ± 0.6	48.5 ± 0.6		
2667	13.3 ± 0.7	27.5 ± 0.6	48.4 ± 0.6		
2665	12.8 ± 0.7	27.3 ± 0.6	48.1 ± 0.6		
2662	12.7 ± 0.7	27.1 ± 0.6	48.6 ± 0.6		
2660	12.8 ± 0.7	26.9 ± 0.6	49.0 ± 0.6		
2657	12.9 ± 0.7	26.9 ± 0.6	48.5 ± 0.6		
2654	13.3 ± 0.7	27.0 ± 0.6	48.8 ± 0.6		
2652	13.9 ± 0.6	27.1 ± 0.6	48.8 ± 0.6		
2649	14.4 ± 0.6	27.2 ± 0.6	49.7 ± 0.7		
2647	14.9 ± 0.6	27.4 ± 0.6	49.5 ± 0.7		

Table S5. CLS triexponential fit parameters for MCM41-OD in pure solvents.

solvent	y_0	A_1	t_1 (ps)	A_2	t_2 (ps)	A_3	t_3 (ps)
CCl_4	0.07 ± 0.01	0.18 ± 0.05	0.8 ± 0.3	0.11 ± 0.02	6 ± 1	0.14 ± 0.01	55 ± 7
Bz	0.12 ± 0.03	0.16 ± 0.08	0.7 ± 0.2	0.22 ± 0.04	7 ± 2	0.23 ± 0.02	37 ± 13

Table S6. FFCF parameters for MCM41-OD in pure solvents.

	T_2 (ps)	Δ_1 (cm^{-1})	τ_1 (ps)	Δ_2 (cm^{-1})	τ_2 (ps)	Δ_3 (cm^{-1})	τ_3 (ps)	Δ_4 (cm^{-1})
CCl_4	0.51 ± 0.3	7 ± 1	0.8 ± 0.3	5.7 ± 0.4	6 ± 1	5.5 ± 0.3	55 ± 7	4.4 ± 0.2
Bz	0.50 ± 0.2	11 ± 1	0.7 ± 0.2	13.1 ± 0.3	7 ± 2	13.6 ± 0.5	37 ± 13	9.8 ± 0.1

References

1. Karthick Kumar, S. K.; Tamimi, A.; Fayer, M. D., Comparisons of 2D IR measured spectral diffusion in rotating frames using pulse shaping and in the stationary frame using the standard method. *J. Chem. Phys.* **2012,** *137* (18), 184201.

2. Hamm, P.; Zanni, M. T., *Concepts and Methods of 2D Infrared Spectroscopy*. Cambridge University Press: New York, 2011; p 286.

3. Shim, S.-H.; Zanni, M. T., How to turn your pump-probe instrument into a multidimensional spectrometer: 2D IR and Vis spectroscopies via pulse shaping. *Phys. Chem. Chem. Phys.* **2009,** *11* (5), 748-761.

4. Shim, S.-H.; Strasfeld, D. B.; Fulmer, E. C.; Zanni, M. T., Femtosecond pulse shaping directly in the mid-IR using acousto-optic modulation. *Opt. Lett.* **2006,** *31* (6), 838-840.

5. Tan, H.-S.; Piletic, I. R.; Fayer, M. D., Polarization selective spectroscopy experiments: methodology and pitfalls. *J. Opt. Soc. Am. B* **2005,** *22* (9), 2009-2017.

6. Yamada, S. A.; Shin, J. Y.; Thompson, W. H.; Fayer, M. D., Water Dynamics in Nanoporous Silica: Ultrafast Vibrational Spectroscopy and Molecular Dynamics Simulations. *J. Phys. Chem. C* **2019,** *123* (9), 5790-5803.

7. Nishida, J.; Tamimi, A.; Fei, H.; Pullen, S.; Ott, S.; Cohen, S. M.; Fayer, M. D., Structural dynamics inside a functionalized metal–organic framework probed by ultrafast 2D IR spectroscopy. *Proc. Nat. Acad. Sci. U.S.A.* **2014,** *111* (52), 18442-18447.

8. Tao, T., Time-dependent fluorescence depolarization and Brownian rotational diffusion coefficients of macromolecules. *Biopolymers* **1969,** *8* (5), 609-632.

9. Tokmakoff, A., Orientational correlation functions and polarization selectivity for nonlinear spectroscopy of isotropic media. I. Third order. *J. Chem. Phys.* **1996,** *105* (1), 1-12.

10. Mukamel, S., *Principles of Nonlinear Optical Spectroscopy*. Oxford UP: New York, 1995.

11. Park, S.; Kwak, K.; Fayer, M. D., Ultrafast 2D-IR vibrational echo spectroscopy: a probe of molecular dynamics. *Laser Phys. Lett.* **2007,** *4* (10), 704.

12. Kwak, K.; Zheng, J.; Cang, H.; Fayer, M. D., Ultrafast Two-Dimensional Infrared Vibrational Echo Chemical Exchange Experiments and Theory. *J. Phys. Chem. B* **2006,** *110* (40), 19998-20013.

13. Kubo, R., A Stochastic Theory of Line-Shape and Relaxation. In *Fluctuation, Relaxation and Resonance in Magnetic Systems*, Ter Haar, D., Ed. Oliver and Boyd: London, 1961.

14. Kwak, K.; Park, S.; Finkelstein, I. J.; Fayer, M. D., Frequency-frequency correlation functions and apodization in two-dimensional infrared vibrational echo spectroscopy: A new approach. *J. Chem. Phys.* **2007,** *127* (12), 124503.
15. Kwak, K.; Rosenfeld, D. E.; Fayer, M. D., Taking apart the two-dimensional infrared vibrational echo spectra: More information and elimination of distortions. *J. Chem. Phys.* **2008,** *128* (20), 204505.
16. Zheng, J.; Kwak, K.; Asbury, J.; Chen, X.; Piletic, I. R.; Fayer, M. D., Ultrafast Dynamics of Solute-Solvent Complexation Observed at Thermal Equilibrium in Real Time. *Science* **2005,** *309* (5739), 1338-1343.
17. Fayer, M. D., Dynamics of liquids, molecules, and proteins measured with ultrafast 2D IR vibrational echo chemical exchange spectroscopy. *Annu. Rev. Phys. Chem.* **2009,** *60*, 21-38.
18. Steinel, T.; Asbury, J. B.; Zheng, J.; Fayer, M. D., Watching Hydrogen Bonds Break: A Transient Absorption Study of Water. *J. Phys. Chem. A* **2004,** *108* (50), 10957-10964.
19. Rezus, Y. L. A.; Bakker, H. J., On the orientational relaxation of HDO in liquid water. *J. Chem. Phys.* **2005,** *123* (11), 114502.
20. Nishida, J.; Fayer, M. D., Guest Hydrogen Bond Dynamics and Interactions in the Metal–Organic Framework MIL-53(Al) Measured with Ultrafast Infrared Spectroscopy. *J. Phys. Chem. C* **2017,** *121* (21), 11880-11890.
21. Carpenter, W. B.; Fournier, J. A.; Lewis, N. H. C.; Tokmakoff, A., Picosecond Proton Transfer Kinetics in Water Revealed with Ultrafast IR Spectroscopy. *J. Phys. Chem. B* **2018,** *122* (10), 2792-2802.
22. Cang, H. Dynamics in Complex Liquids. Stanford University, 2004.
23. Ji, M.; Odelius, M.; Gaffney, K. J., Large Angular Jump Mechanism Observed for Hydrogen Bond Exchange in Aqueous Perchlorate Solution. *Science* **2010,** *328* (5981), 1003.
24. Berne, B. J.; Pecora, R., *Dynamic Light Scattering: With Applications to Chemistry, Biology, and Physics*. Dover: New York, 2000.
25. Zheng, J.; Fayer, M. D., Solute−Solvent Complex Kinetics and Thermodynamics Probed by 2D-IR Vibrational Echo Chemical Exchange Spectroscopy. *J. Phys. Chem. B* **2008,** *112* (33), 10221-10227.